Instabilities and turbulence in low-β guide field reconnection exhausts with kinetic Riemann simulations

Cite as: Phys. Plasmas **26**, 102115 (2019); https://doi.org/10.1063/1.5121782
Submitted: 27 July 2019 . Accepted: 01 October 2019 . Published Online: 22 October 2019

Qile Zhang, J. F. Drake, and M. Swisdak

Physics of Plasmas ARTICLE scitation.org/journal/php

Instabilities and turbulence in low-β guide field reconnection exhausts with kinetic Riemann simulations

Cite as: Phys. Plasmas **26**, 102115 (2019); doi: 10.1063/1.5121782
Submitted: 27 July 2019 · Accepted: 1 October 2019 ·
Published Online: 22 October 2019

Qile Zhang, J. F. Drake, and M. Swisdak

AFFILIATIONS

Institute for Research in Electronics and Applied Physics, University of Maryland, College Park, Maryland 20742, USA

ABSTRACT

The role of turbulence in low-β, guide-field reconnection exhausts is explored in 2D reconnection and 2D and 3D Riemann simulations. The structure of the exhaust and associated turbulence is controlled by a pair of rotational discontinuities (RDs) at the exhaust boundary and a pair of slow shocks (SSs) that are generated by counterstreaming ions beams. In 2D, the exhaust develops large-amplitude striations at the ion Larmor radius scale that are produced by electron-beam-driven ion cyclotron waves. The electron beams driving the instability are injected into the exhaust from one of the RDs. However, in 3D Riemann simulations, the additional dimension (in the out-of-plane direction) results in strong Buneman and electron-electron streaming instabilities at the RD which suppress the electron beam formation and therefore the striations in the exhaust. The strength of the streaming instabilities at the RD is controlled by the ratio of the electron thermal speed to Alfvén speed, with the lower thermal speed being more unstable. In the 3D simulations, an ion-ion streaming instability acts to partially thermalize the counterstreaming ion beams at the SSs. This instability is controlled by the ratio of the sound speed to Alfvén speed and is expected to be stable in the low β solar corona. The results suggest that in a guide field reconnection exhaust with $1 \gg \beta > m_e/m_i$, the kinetic-scale turbulence that develops will be too weak to play a significant role in energy conversion and particle acceleration. Therefore, the energy conversion will be mostly controlled by laminar physics or multi-x-line reconnection.

I. INTRODUCTION

Magnetic reconnection and turbulence are fundamental processes in plasma systems. Reconnection converts magnetic energy to plasma high speed flows, heating, and energetic particles through a change of the magnetic topology. Turbulence contributes to particle scattering, transport, acceleration, energy dissipation, and so on. These two phenomena could intertwine, so it is of fundamental importance to understand the role of turbulence in reconnection, especially in the process of energy conversion.

Here, we focus our attention on turbulence in single x-line reconnection rather than multi x-line reconnection. Turbulence is often driven by instabilities. Previous observational and numerical studies have investigated instabilities and turbulence in reconnection near the diffusion region and along the magnetic separatrices that emanate from the magnetic x-line[1–7] as well as in the exhaust downstream of the x-line.[8–12] They could contribute to anomalous resistivity and viscosity, cause dissipation and scattering, and so on. The major region of energy conversion is the reconnection exhaust downstream of the x-line. Recently, Eastwood *et al.*[11] observed a guide field reconnection exhaust ~100 d_i (with d_i being the ion inertial length) downstream of the x-line with a β of order unity and identified electron holes. Muñoz and Büchner[9] used low-β (<0.1) 2D particle-in-cell (PIC) simulations to explore the turbulence present in guide field reconnection exhausts. However, the simulation domains only extended about 6 d_i downstream of the x-line so the turbulence further downstream remains to be explored. In this paper, we will also focus on the guide field and the low-β regime, which is relevant to the solar corona and the inner heliosphere, where reconnection can drive powerful releases of magnetic energy in solar flares and coronal mass ejections (CMEs).

To study the exhaust, 2D PIC reconnection simulations are usually used to capture the kinetic effects. However, simulations of large systems at a low β with a sufficiently high ion-to-electron mass ratio are computationally expensive, so we employ the PIC Riemann simulation model. The magnetic geometry of a Riemann simulation resembles a single reconnection outflow downstream of the x-line without capturing the reconnection process near the x-line. A Riemann simulation reduces the dimension of an 2D outflow by neglecting the slow variation in the outflow direction (x), so it becomes one dimensional (along y) in its most basic formulation.[13] The computational cost to carry out PIC Riemann simulations is therefore greatly reduced

compared with PIC 2D reconnection simulations and we can consequently explore systems with a much larger spatial domain in y and z. However, to capture kinetic-scale instabilities and turbulence, a small length in the outflow (x) or guide field (z) direction can be kept, resulting in 2D or 3D Riemann simulations. Previously, 2D (x-y) Riemann simulations have been used to model the instabilities and turbulence of antiparallel reconnection exhausts using either hybrid[14–16] or PIC[17,18] models.

In an earlier paper, we explored the structure of reconnection exhausts in the low-β, strong-guide-field limit using PIC Riemann simulations.[19] We showed that the exhaust was bounded by rotational discontinuities (RDs) with parallel slow-shocks (SSs) forming within the exhaust as expected from the magnetohydrodynamic (MHD) model.[13] This differs from the structure in the weak guide-field case, where the exhaust is bounded by Petschek-like switch-off slow shock/rotational discontinuity compound structures.[8,20,21] The SSs in our simulations remained laminar and were not effective in heating either electrons or ions through the usual diffusive shock acceleration mechanism. In this paper, we explore in much greater depth the instabilities and turbulence in low-β guide field reconnection exhausts to reveal the parameter regimes in which the reconnection exhausts are laminar or turbulent. We carry out a 2D reconnection simulation and 2D and 3D Riemann simulations with various mass ratios.

The guide field breaks the system's symmetry and leads to a density cavity at the RD on one side of the exhaust (the side where the electron velocity supporting the current across the RD points toward the midplane of the exhaust) and a density bump at the other RD. In 2D simulations, the streaming electrons in the cavity of the RD drive the Buneman instability at an early time, but later in time, the dominant instability moves to the core of the exhaust and leads to large amplitude striations in the parallel current with characteristic scales of the order of the ion Larmor radius ρ_i. The instability is an ion cyclotron wave driven by the strong electron beam injected into the exhaust by the low density RD.[22] However, in 3D simulations, the Buneman instability as well as the electron-electron streaming instability at the low density RD become much stronger (due to a nonzero k_z), so that the electron beam injected into the exhaust becomes much weaker and the development of the striations is suppressed. The result points to the importance of full 3D simulations of reconnection to understand the mechanisms for energy conversion. The strength of the streaming instabilities at the RD is controlled by the ratio of the electron thermal speed to Alfvén speed, with the lower thermal speed being more unstable. The 3D simulations also reveal the development of a weak ion-ion streaming instability within the exhaust that did not appear in the 2D model. This instability partially thermalizes the counterstreaming ion beams at the SSs. This weak instability is expected to be stabilized at a lower beta where the ion relative drift (of the order of Alfvén speed) becomes larger than the sound speed. As a result, the counterstreaming ion beams that develop during the low-β, guide field reconnection can propagate long distances without thermalizing. The conclusion, therefore, is that in the regime $1 \gg \beta > m_e/m_i$, the instabilities and turbulence that develop are expected to be weak in a realistic guide-field reconnection exhaust. The dynamics of a single x-line exhaust is therefore dominated by laminar processes in this regime.[19]

The organization of the paper is as follows: in Sec. II, we present the results of the simulations of 2D reconnection exhausts, including a discussion of turbulence; in Sec. III, we present the results of the 2D Riemann simulations and analyze the associated turbulence; in Sec. IV, we present the results of the 3D Riemann simulations and show that there are qualitative differences between 2D and 3D simulations and modest vs large mass-ratio simulations; and in Sec. V, we present the conclusions and implications.

II. INSTABILITIES AND TURBULENCE IN 2D RECONNECTION EXHAUSTS

In this paper, we perform simulations using the particle-in-cell code `p3d`.[23] The particles are advanced by the Newton-Lorentz equations of motion and the fields by Maxwell's equations. We apply periodic boundary conditions to all boundaries, so we have two identical reconnection current sheets to achieve the periodic condition in y. However, we only focus on one current sheet in half of the domain. Here, the magnetic field strengths are normalized to the initial asymptotic field in the x direction $B_{x,a}$, densities to the initial asymptotic density n_0, lengths to the ion inertial length $d_i = c/\omega_{pi}$ based on n_0, times to the inverse ion cyclotron frequency Ω_{ci}^{-1}, velocities to the Alfvén speed C_{Ax} based on $B_{x,a}$ and n_0, and temperatures to $m_i C_{Ax}^2$. In this section, we show results from a 2D guide field reconnection simulation (run 1) with a guide field equal to the reconnecting field ($B_{z,a} = B_{x,a}$), which is initialized by a force free configuration

$$B_x = B_{x,a} \tanh(y/w_0), \tag{1a}$$

$$B_z = \sqrt{(B_{x,a}^2 + B_{z,a}^2 - B_x^2)}, \tag{1b}$$

$$n = n_0. \tag{1c}$$

Other parameters are shown in Table I. This simulation has an initial total β of 0.1. In this paper, the number of particles per grid cell (ppg) is 100 in 2D simulations and is 25 in 3D simulations. Besides, a B_y perturbation highly localized in x is used to initiate a single x-line in the initial current sheet. The perturbation takes the form: $\delta B_y = \partial_x((\sin(2\pi x/L_x))^{499})$.

This simulation creates a steady reconnection exhaust extending for more than 100 d_i along the outflow direction as shown in Fig. 1. This simulation was also analyzed in Zhang *et al.*[19] with emphasis on the heating and the overall structure. Here, we focus on the instabilities

TABLE I. Simulation parameters.

Run	m_i/m_e	$B_{x,a}$	$B_{z,a}$	$T_i = T_e$	dims	$L_y \times L_x \times L_z$	c^2	dx	dt	ppg
1	25	1	1	0.05	2	$102.4 \times 409.6 \times 0$	45	0.0125	5.9×10^{-3}	100
2	25	1	1	0.05	2	$102.4 \times 16 \times 0$	45	0.0125	5.9×10^{-3}	100
3	25	1	1	0.05	3	$32 \times 8 \times 8$	45	0.0125	5.9×10^{-3}	25
4	100	1	1	0.05	3	$32 \times 4 \times 2$	180	0.00625	2.95×10^{-3}	25

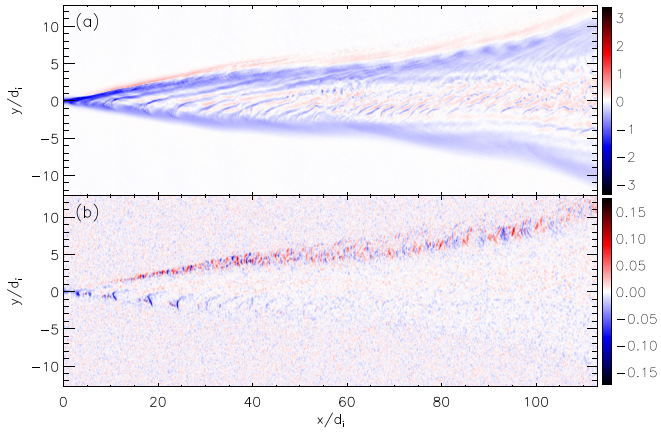

FIG. 1. $J_{\|}$ (a) and $E_{\|}$ (b) of a reconnection exhaust in the 2D reconnection simulation run 1.

and turbulence. In Fig. 1(a), we show the parallel current $J_{\|} = \mathbf{J} \cdot \mathbf{B}/B$, which is mostly carried by electrons. We see the two current sheets bounding the exhaust which are the RDs.[19] Note that they are not the separatrices but are downstream of the separatrices since there is no change of the magnetic topology across them. The core of the exhaust is highly structured with oblique striations in the current. When these striations first develop downstream of the x-line, the source is from the low density RD. Further downstream, the core of the exhaust becomes more turbulent and this turbulence appears to be disconnected from the RD. In Fig. 1(b), we show the parallel electric field $E_{\|} = \mathbf{E} \cdot \mathbf{B}/B$, which indicates the ongoing instabilities at both RDs. Those at the bottom RD are strong close to the x-line and fade away further downstream. The fluctuations develop at a short scale close to the x-line and then clump to larger scales that link to the striations within the exhaust. The nature of these instabilities and turbulence is discussed in Sec. III.

III. STUDIES OF INSTABILITIES AND TURBULENCE USING 2D RIEMANN SIMULATIONS

A. Riemann simulations to explore reconnection exhausts

To study the current striations and instabilities in the reconnection exhaust in greater detail, we first simplify the configuration by using Riemann simulations. As has been discussed previously,[8,13,14,19] Riemann simulations model the reconnection exhaust by neglecting the dependence on the outflow direction x. Here, since we want to study the structures and instabilities in the x-y plane as in the reconnection simulation, we maintain a long enough length in the x dimension to model the striations. Thus, the 2D Riemann simulation is performed in an x-y domain. The parameters (see run 2 in Table I) and initial profiles are almost the same as run 1 but there is a small initial magnetic field $B_y = 0.1B_{x,a}$ added so that the magnetic tension can drive the outflow. In addition, the half width in y of the initial current sheet w_0 is chosen to be close to the half width of the x-line current sheet in run 1 at the time of Fig. 1. The Riemann simulation result at time t is a proxy of the reconnection exhaust region at a distance $C_{Ax} * t$ downstream from the x-line. Zhang *et al.*[19] demonstrated that Riemann simulations capture the overall structure of the reconnection exhaust. Here, we show that they also capture the development of turbulence and hence can be used as proxies for full simulations to study that turbulence.

We first show the overall 1D profiles (averaged over x) of the 2D Riemann simulation in Fig. 2. In Fig. 2(a), there are two locations where the magnetic field rotates from the dominant x-z direction to the z direction. These rotations form the RDs that bound the exhaust. We also plot the initial magnetic field profiles in dashed lines for comparison. In Figs. 2(b) and 2(c), we present the three velocity components of the electrons and ions. The RDs drive the exhaust velocity V_x of both species. The RDs also drive out-of-plane plasma fluid flows V_z that are seen most easily in the ions. These flows are toward the midplane of the exhaust and in the MHD model produce the SSs that develop in guide field reconnection. The RDs are supported by a current J_z that produces the magnetic rotation. From Ampère's law, the direction of J_z is the same (negative) at both RDs. The electrons have a larger positive V_z than the ions (to create a negative J_z), so the electrons dominate the current at the RD. Since B_z and B_y are both positive across the domain [Fig. 2(a)], the electrons with a positive v_z at both RDs flow along the field line toward the positive y direction. So the electrons that carry the current at the left RD are at the same time accelerated into the exhaust. The acceleration reduces the local density due to flux continuity and creates a density cavity at the left RD [Fig. 2(d)]. In contrast, the electrons that carry the current at the right RD are accelerated away from the exhaust, leading to a pileup of the electrons and therefore a density increase. These density variations at the RDs have no counterpart in MHD.

In Fig. 3, we show the results from this 2D Riemann simulation at both early and late times, as proxies of regions of about 25 d_i and 100 d_i downstream of the x-line in the reconnection simulation in Fig. 1. Although $L_x = 16$ in this simulation, we only show half the domain with $x \in [0,8]$ to facilitate the comparison to a 3D simulation of a smaller domain shown later in Fig. 7. Figs. 3(a) and 3(b) show $J_{\|}$ and Figs. 3(c) and 3(d) show $E_{\|}$. Compared to Fig. 1, we see that the

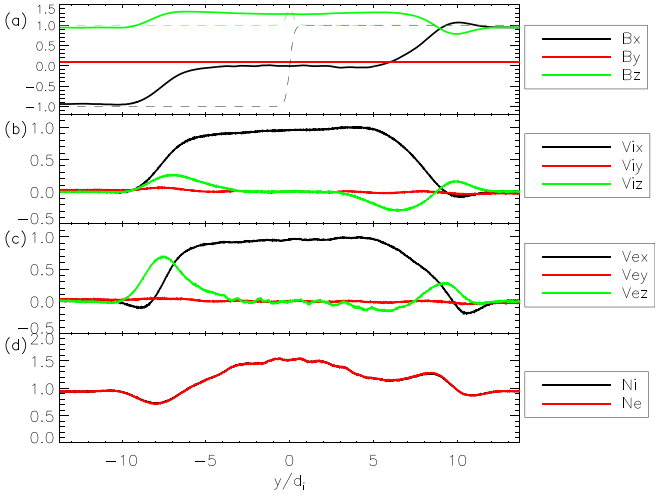

FIG. 2. The overall 1D profiles (averaged over x) of the 2D Riemann simulation (run 2). (a) The magnetic fields (with the initial profiles in dashed lines of the same color), (b) ion velocities, (c) electron velocities, and (d) ion and electron densities (which nearly overlap).

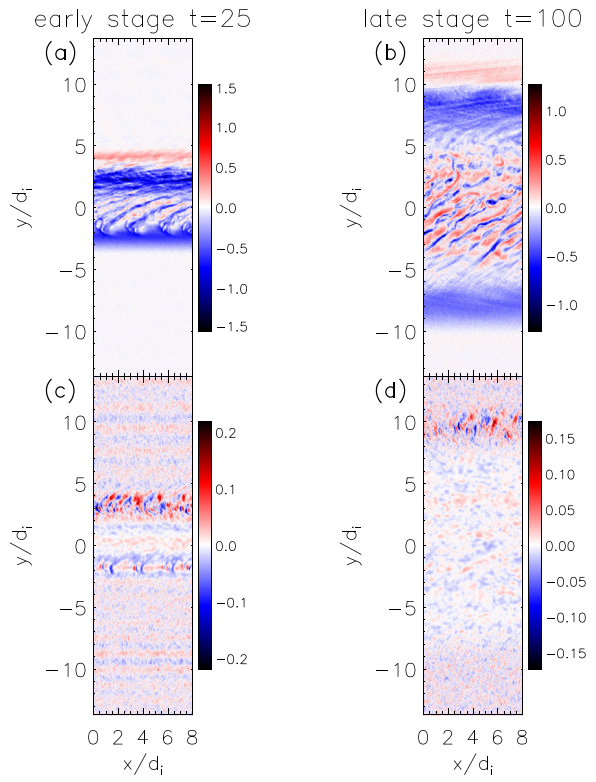

FIG. 3. (a) and (b) $J_{\|}$ and (c) and (d) $E_{\|}$ at two times from the 2D Riemann simulation (run 2).

Riemann simulation captures all the essential features of the instabilities and turbulence we discussed in the 2D reconnection simulation, including the oblique current striations and the structuring of $E_{\|}$. The amplitudes of these fluctuations are also comparable to those in the reconnection simulation. This suggests that the Riemann simulations can be used to explore the development of turbulence in reconnection exhausts. Therefore, we will use Riemann simulations to explore the nature of these instabilities and the development of turbulence.

B. Studies of instabilities and turbulence

In Fig. 4, we show the early evolution of the Riemann simulation to understand the dynamics just downstream of the x-line. Shown are the data from times $t = 5$, 10, and 15. Figures 4(a)–4(c) show $J_{\|}$, and Figs. 4(d)–4(f) show $E_{\|}$. In Fig. 4(d), the instability in the bottom current sheet is still in, or just past, its linear phase. Correspondingly, the current in Fig. 4(a) is modified by the instability and the striations in the current begin to extend from this current sheet into the exhaust. The reason why the current sheet on this side affects the current structures in the exhaust is that the current here is supported by electrons flowing toward the midplane, as discussed in Sec. III A. So the structures of the current at this RD convect into the exhaust. Since the exhaust outflow is in the positive x direction relative to the almost stationary upstream plasma [Fig. 2(c)], there is a velocity shear that the electrons will experience when they flow from the current sheet into the exhaust. That is why the striations tilt toward the positive x direction. We also show the phase space x-$V_{\|}$ in Fig. 4(g) which is taken along the green dotted line in Fig. 4(d). The ion population is in red and the electron population is in blue. Their maximum phase space densities are normalized to be the same. Since both species are strongly modified by the instability, we conclude that the instability is an oblique Buneman instability. This instability can develop in this 2D system with a wave vector k_x because the current has an x component. The wave vector in z cannot develop in this 2D x-y simulation. As a cross-check, we verified that the dominant k_x was consistent with the prediction for the Buneman instability in Drake *et al.*,[1]

$$k = \delta\omega_{pe}/v_{de}, \tag{2}$$

where $\delta^2 = (1 + \sin^2\theta\omega_{pe}^2/\Omega_{ce}^2)^{-1}$. By evaluating the local parameters, electron beam speed $v_{de} = 2$, wave vector direction relative to the field $\cos\theta = 0.3$, density $n = 0.5$, and magnetic field $B = 1.4$, we calculate the wavelength along x to be 0.6, which matches that found in the simulation.

In Figs. 4(e) and 4(f), the turbulence at the bottom RD evolves to a longer wavelength, forming well-separated, large-scale structures that drive the electron current striations into the core of the exhaust. To understand why the core of the exhaust become more turbulent further downstream and to further clarify how the striations develop in the lower RD, we show in Fig. 5 the phase space y-$V_{\|}$ for ions and electrons along a cut in y (at $x = 4$ and $t = 100$) across the exhaust. We see from the electrons in Fig. 5(b) that the instability at the cavity RD (on the left) is weak, so the electron beam flows into the exhaust without dissipation when crossing the RD. After being accelerated into the exhaust, the beam becomes unstable, driving the turbulence in the exhaust. This instability has $\omega \sim \Omega_{ci}$, $k\rho_i \sim 1$. Since the local magnetic field is dominantly in the out-of-plane direction ($B_x \sim 0$ and $B_z/B_y \sim 13$), this instability's in-plane wave vector is very oblique to the magnetic field ($\cos\theta = 0.054$). To determine the nature of this local instability, we analyze the electrostatic dispersion relation similar to Drummond and Rosenbluth[22] in terms of the plasma dispersion function Z as below:

$$\sum_j \sum_{n=-\infty}^{\infty} \frac{\Gamma_n(k_\perp^2\rho_j^2)}{(k\lambda_{Dj})^2}\left\{\frac{1}{2}Z'\left(\frac{\omega - k_{\|}u_j - n\Omega_j}{k_{\|}v_j}\right) - \frac{n\Omega_j}{-\omega + k_{\|}u_j + n\Omega_j}\left[1 + \frac{1}{2}Z'\left(\frac{\omega - k_{\|}u_j - n\Omega_j}{k_{\|}v_j}\right)\right]\right\} = 1. \tag{3}$$

Here, $\Gamma_n(x) = e^{-x}I_n(x)$, $I_n(x)$ is the modified Bessel function of the first kind, $Z'(s)$ is the derivative of the Z function with $Z'(s) = -2(1 + sZ(s))$. The subscript j stands for the different species, v_j is the thermal speed, Ω_j is the cyclotron frequency, $\rho_i = v_j/\Omega_j$ is the Larmor radius, $\lambda_{Dj} = v_j/\omega_{pj}$ is the Debye length where ω_{pj} is the plasma frequency of species j, and u_j is the drift speed. $k_{\|} = k\cos\theta$ is the parallel component of the wave vector and $k_\perp = k\sin\theta \approx k$ is the perpendicular component. We use this dispersion relation to examine a simplified system with three populations: one electron beam (labeled as eb), one lower energy electron population (ec), and one ion population (i), which is analogous to the distributions in Fig. 5(b) at around $y = -4$. For simplicity, these populations are assumed to be isotropic Maxwellian distributions and have temperatures close to their parallel temperatures in the simulation. The ion population has density one, temperature 0.05, and speed zero. The electron beam has density 0.3,

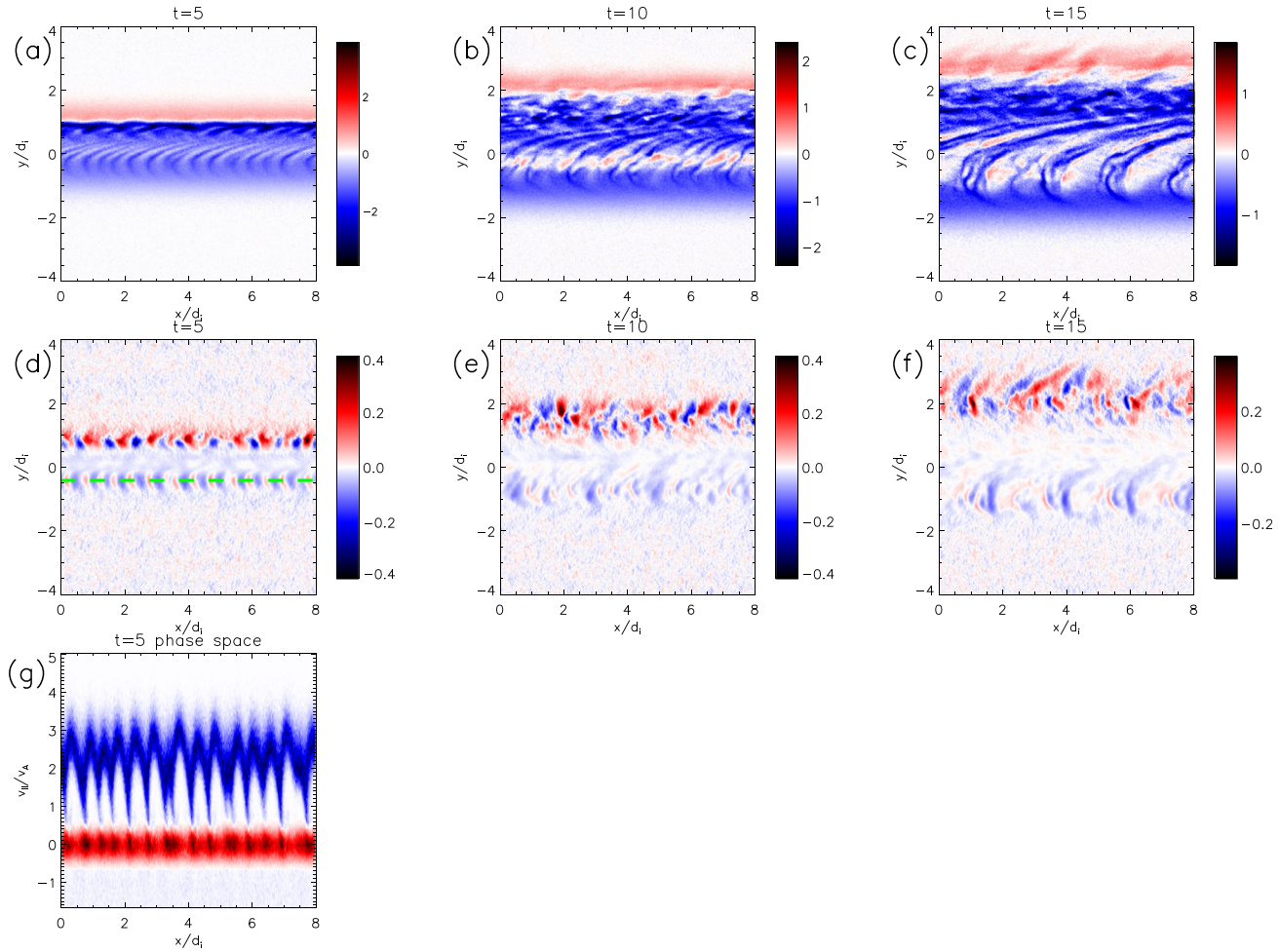

FIG. 4. The early evolution from run 2. In (a)–(c), $J_\parallel$ and in (d)–(f), $E_\parallel$. In (g), the phase space x-$V_\parallel$ which is taken along the green dotted line in (d). The ion population is shown in red and the electron population is shown in blue, with their maximum phase space densities normalized to be the same.

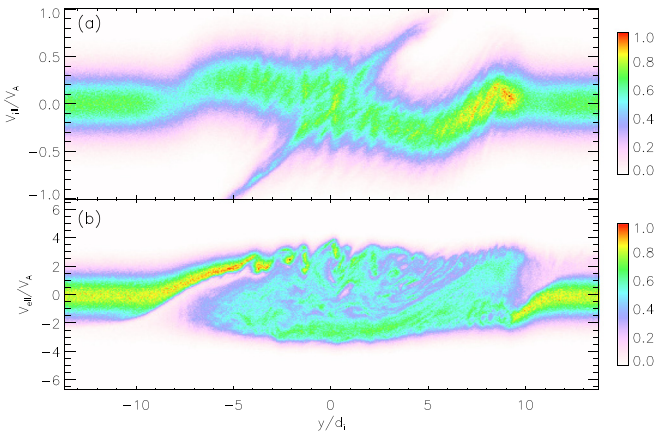

FIG. 5. The phase space y-$V_\parallel$ for ions (a) and electrons (b) along a cut in y across the exhaust of run 2 at x = 4 and t = 100. The color bar is normalized to the maximum value in each panel.

temperature 0.005, and speed 2.5. The lower energy electron population has density 0.7, temperature 0.08, and speed $-2.5 \times 0.3/0.7 = -1.07$ to ensure zero current. The total magnetic field is about 1.3. We keep the $|n| \leq 1$ terms in the sum over the Bessel function harmonics and use $k_\parallel v_i \ll \omega \sim \Omega_i$, $\Omega_e \gg k_\parallel v_e$, and $k_\perp^2 \rho_e^2 \ll 1$ to reduce the relation to

$$\frac{\Gamma_1(k_\perp^2\rho_i^2)}{(k\lambda_{Di})^2}\frac{\Omega_i}{\omega-\Omega_i} - \frac{\Gamma_1(k_\perp^2\rho_i^2)}{(k\lambda_{Di})^2}\frac{\Omega_i}{\omega+\Omega_i} + \frac{1}{2(k\lambda_{Deb})^2}Z'\left(\frac{\omega-k_\parallel u_{eb}}{k_\parallel v_{eb}}\right) + \frac{1}{2(k\lambda_{Dec})^2}Z'\left(\frac{\omega-k_\parallel u_{ec}}{k_\parallel v_{ec}}\right) - \frac{\omega_{pe}^2}{\Omega_e^2} = 1, \quad (4)$$

where ω_{pe} is the electron plasma frequency based on the total electron density. We numerically solve this dispersion relation and plot the solution ω and γ vs k in Figs. 6(a) and 6(b). The growth rate reaches its maximum at around $k = 1.6$ and slowly decreases at a higher k. We have also used a kinetic dispersion relation solver `pdrk`[24] to solve the full electrostatic dispersion relation involving the three populations

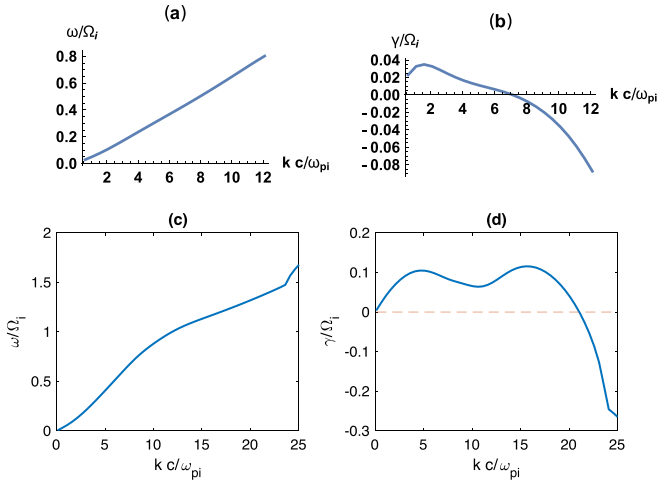

FIG. 6. The solution ω (a) and γ (b) vs k from the dispersion relation in Eq. (4). In (c) and (d), the solution of the full electromagnetic dispersion relation using the solver `pdrk`.[24]

above and we get qualitatively similar results. For the unstable modes around the maximum growth k, the dominant terms in the simplified dispersion relation are the first four terms: two ion terms, one electron beam term, and one lower energy electron term. We also tried neglecting the second ion term in the dispersion relation [proportional to $(\omega+\Omega_i)^{-1}$] and found that the result is qualitatively unchanged, so the first ion term [the ion cyclotron term proportional to $(\omega-\Omega_i)^{-1}$] and the other two electron terms are dominant. These three terms coupled together suggest that this is an oblique ion cyclotron instability driven by the electron beam, which is similar to the instability discussed in Drummond and Rosenbluth.[22] The fact that the instability is driven by the electron beam in these 2D simulations is also supported by the results of 3D simulations presented later in which the electron beam is suppressed and the instability is absent. In comparison to the simulation, the k value measured in the simulation is around 5, which is several times larger than the k with the maximum growth rate from this simplified dispersion relation. This is due to the electromagnetic effects. In fact, we have used `pdrk` to solve the full electromagnetic dispersion relation and show the results in Figs. 6(c) and 6(d). As seen in Fig. 6(d), there is a maximum growth peak at around $k=5$, in a good agreement with the simulation. However, there is also another

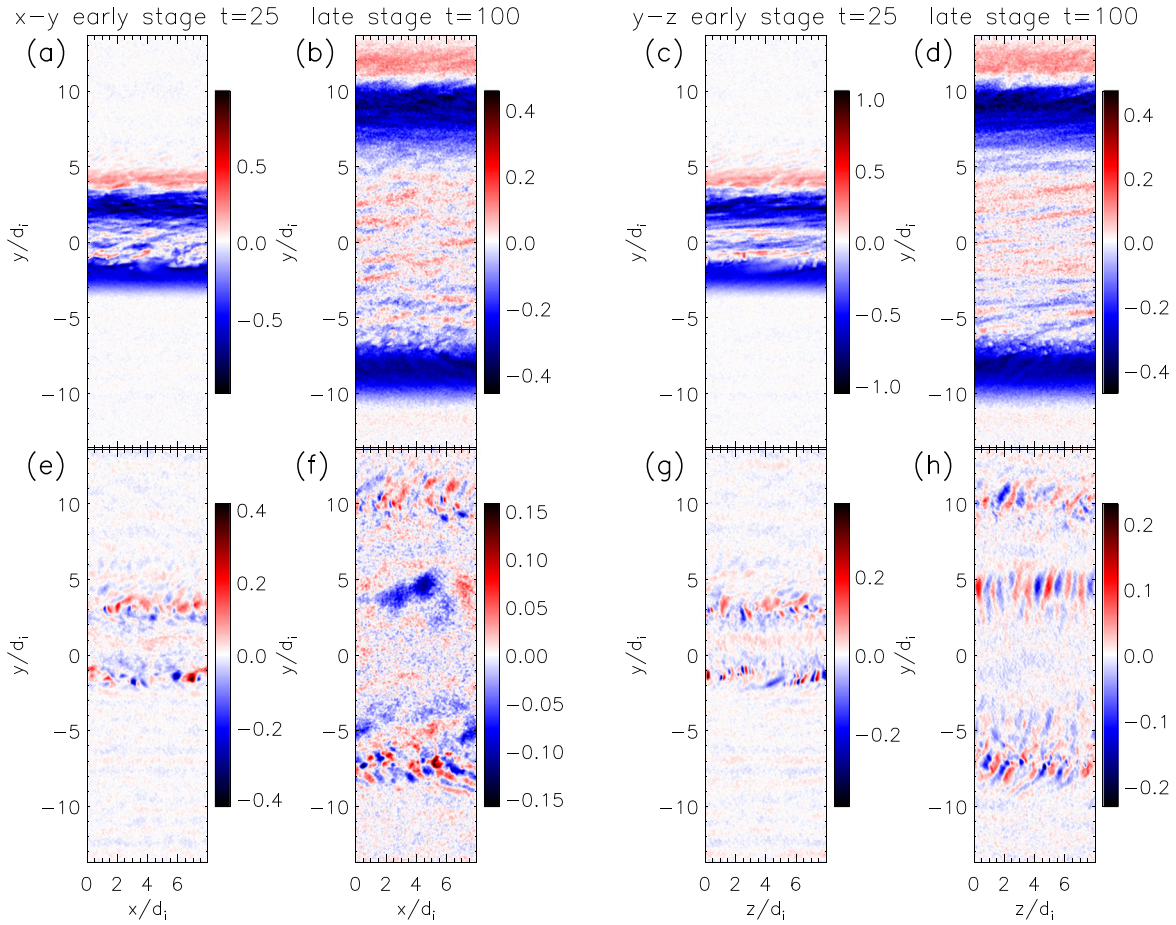

FIG. 7. The 2D cuts (x-y and y-z) from run 3 through the middle of the 3D domain at $z=4$ and $x=4$, respectively. In (a) and (b), x-y cuts of $J_\parallel$ and in (c) and (d), y-z cuts of $J_\parallel$. In (e) and (f), x-y cuts of $E_\parallel$ and in (g) and (h), y-z cuts of $E_\parallel$.

peak at around $k = 15$, which can also be found using the pdrk electrostatic mode. However, due to their typically higher saturation amplitudes, longer wavelength modes dominate late time dynamics. We conclude therefore that the striations in the exhaust core are electromagnetic, electron-beam-driven ion cyclotron waves.

We have used the 2D Riemann simulation as a proxy to understand the physics of instabilities and turbulence that develop in the 2D reconnection simulation. However, the 2D limitation forces the instability wave vector in these simulations to be oblique to the magnetic field and thus these simulations may not capture the true nature of the instabilities and turbulence in a real 3D system. Yet a 3D reconnection simulation is too computationally expensive to accommodate an exhaust extending far downstream of the x-line. We therefore use 3D Riemann simulations to explore the development of turbulence in 3D reconnection exhausts.

IV. 3D RIEMANN SIMULATIONS

A. Comparison to 2D

In Fig. 7, we present the results of a 3D Riemann simulation (run 3) with $L_x = L_z = 8, L_y = 32$ and a reduced number of particles per grid, but otherwise, the same physical parameters as run 2. The data is presented in 2D cuts (either x-y or y-z) through the middle of the 3D domain, which is at $z = 4$ and $x = 4$. Due to the lower ppg and higher noise in 3D simulations, each 2D image from 3D simulations shown in this paper is smoothed three times in succession in both dimensions with a 5-point boxcar stencil. First, the instabilities exhibit large values of k_z, which could not exist in the 2D simulation. This means that 2D simulations in the x-y plane are not adequate to explore the dynamics of these instabilities. Within the exhaust, the magnetic field is dominantly in the z direction so the results of Fig. 7 are evidence that wavevectors parallel to the ambient magnetic field are needed to properly describe the turbulence that develops within the exhaust. A surprise from the data in Figs. 7(a) and 7(b) is that the oblique current striations within the exhaust described previously become weak. The data in Figs. 7(g) and 7(h) reveal the growth of strong instabilities with finite k_z at both RDs and within the core of the exhaust. At late time in Fig. 7(h), the instability in the bottom (low density) RD does not weaken as it did in 2D [Fig. 3(d)]. The instability within the exhaust around $y = 5$ in Fig. 7(h) was not present in the 2D simulation.

The ion and electron phase spaces $y - V_{\|}$ from the run 3 simulation at $t = 100$ are shown in Fig. 8. The cuts are along a line in y across the exhaust at $x = 4$ and $z = 4$. We plot dotted lines in Figs. 8(a) and 8(b) to indicate the y location where the amplitudes of the dominant instabilities peak. The line in Fig. 8(a) at $y = 5$ marks the location of

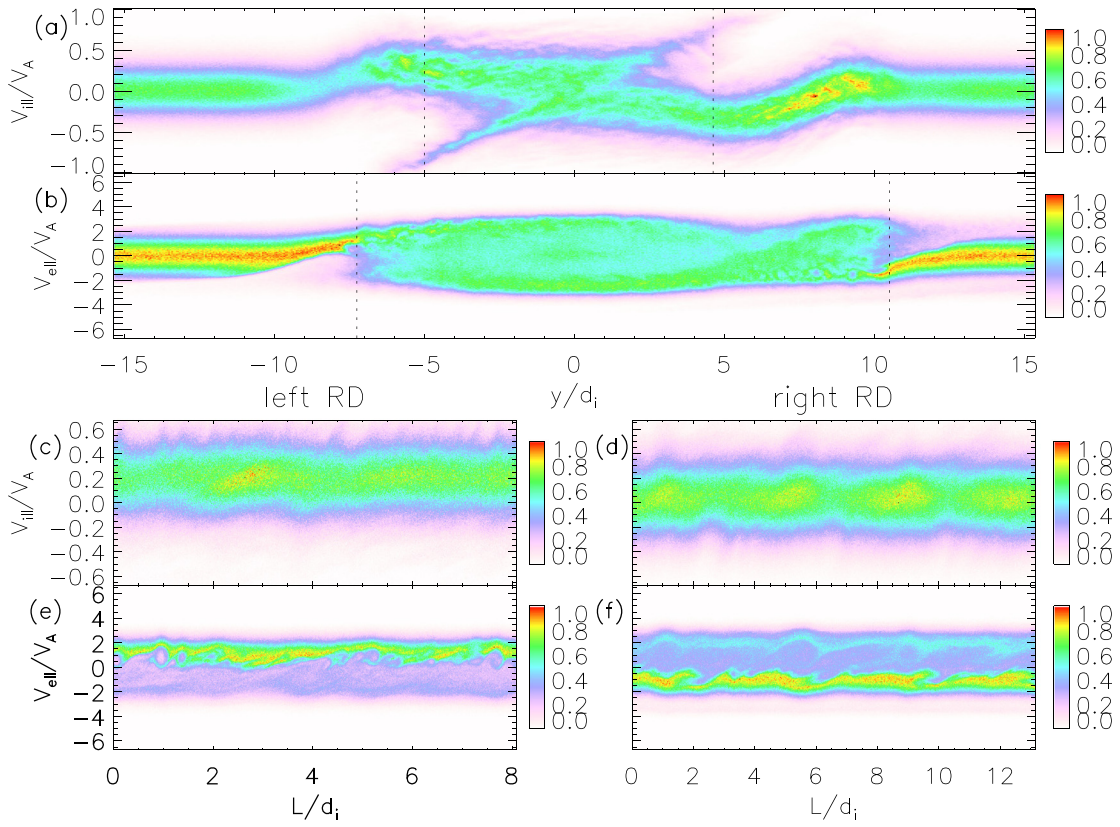

FIG. 8. In (a) and (b), the ion and electron y-$V_{\|}$ phase space from run 3 along a line in y across the exhaust at $x = 4$ and $z = 4$. The dotted lines in (a) and (b) indicate the y location where the instabilities are peaked. The two lines in (a) are for the instability in the core of the exhaust. The other two lines in (b) are for the instabilities at both RD current sheets. The parallel phase space L-$V_{\|}$ along the field lines at these two y locations for ions and electrons are shown in (c)–(f), where L is the distance along the field starting from $x = 0, z = 0$ along the positive z direction. The color bar is normalized to the maximum value in each panel.

the new instability in the core of the exhaust. It is an ion-ion streaming instability that is driven by the counterstreaming ions that are evident in the ion phase space. The instability is also more weakly driven around $y = -5$. This instability is the strongest around the locations of the SSs. This instability will be discussed in depth later in the context of a mass ratio 100 simulation. The two lines in Fig. 8(b) are for the instabilities at the RD current sheets. We show the parallel phase space L-$V_{\parallel}$ along the field lines at these two y locations for ions and electrons in Figs. 8(c)–8(f), where L is the distance along the magnetic field starting from $x = 0, z = 0$ and moving in the positive z direction. The field line here is assumed to lie in the x-z plane, since B_y is an order of magnitude smaller than the total field strength. The correlated structuring of the ion beam and two electron beams in the phase spaces along the direction of the magnetic field show that they are a mixture of Buneman and electron-electron streaming instabilities. They result from the relative drifts between the current-supporting electron beam and the other ion or electron populations. These strong instabilities at the low density RD dissipate the current-supporting electron beam more efficiently than in the 2D simulation [compare Fig. 5(b) with Fig. 8(b)] and prevent it from forming the current striations in the exhaust core.

B. The impact of the mass ratio on the development of turbulence

The results of a 3D Riemann simulation with mass ratio 100 (run 4) with a domain of $L_x = 4, L_z = 2$ are presented in Fig. 9. The other parameters of the simulation are identical to those of run 3. Thus, the data from the two simulations can be compared to establish the sensitivity of turbulence drive mechanisms to the artificial mass ratio in the simulations. The data is organized in Fig. 9 in the same way as in Fig. 7, and with the same color bar for each corresponding panel. The x-y and y-z cuts are also through the middle of the 3D domain, which is at $z = 1$ and $x = 2$. Note that we do not respect the image aspect ratio here since the dimensions x and z would be too short to clearly display the results. The plots displaying $E_{\parallel}$ reveal that the instabilities develop at a shorter wavelength in the mass-ratio 100 run. For the Buneman and electron-electron streaming instabilities at the two RDs, this is consistent with the expected scaling $k \sim \omega_{pe}/v_{de}$. The turbulence at the RDs is also less well developed in the mass-ratio 100 run, indicating that the turbulence is weaker. For a lower electron mass, the electron thermal speed increases while the current and therefore the electron drift speed needed to support the RD does not. Thus, the ratio

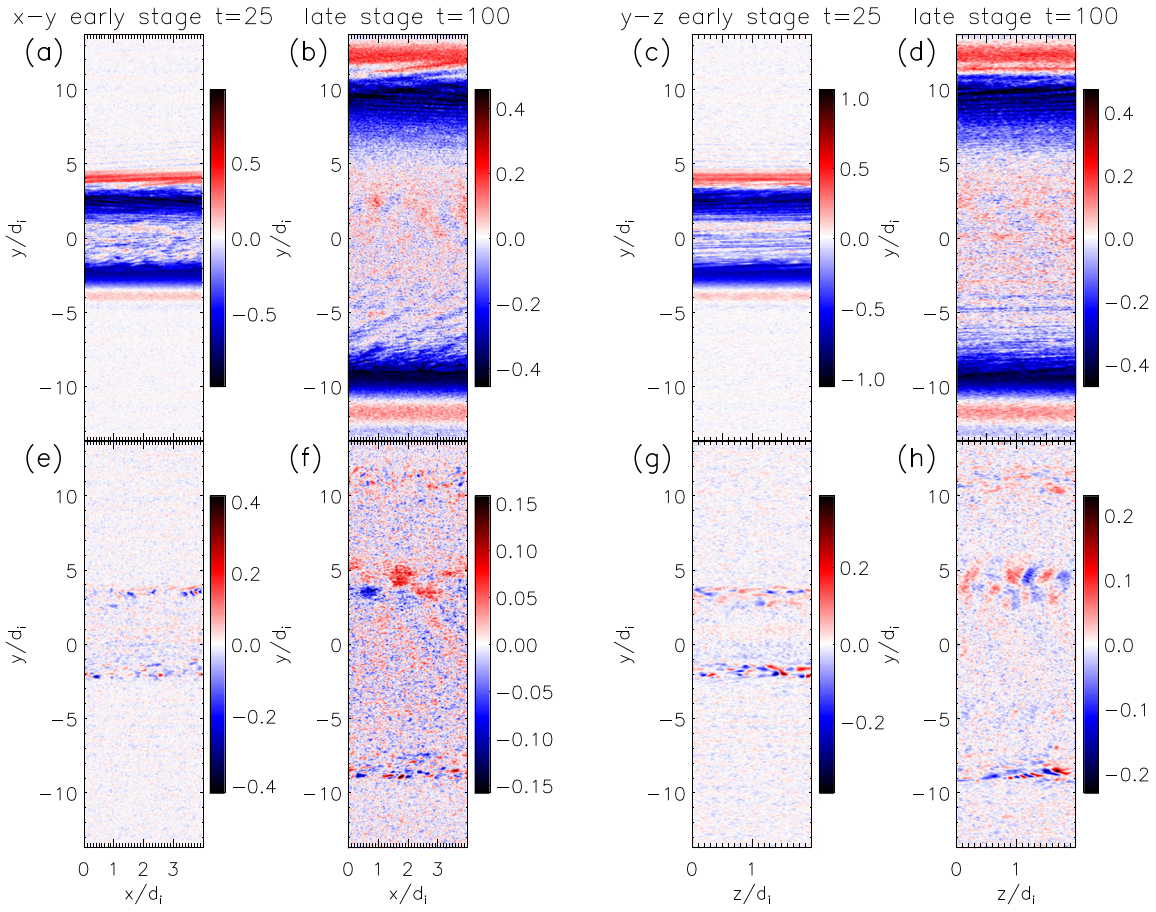

FIG. 9. The 2D cuts (x-y and y-z) from run 4 through the middle of the 3D domain at $z = 1$ and $x = 2$, respectively. In (a) and (b), x-y cuts of $J_{\parallel}$ and in (c) and (d), y-z cuts of $J_{\parallel}$. In (e) and (f), x-y cuts of $E_{\parallel}$ and in (g) and (h), y-z cuts of $E_{\parallel}$. These quantities are organized in the same way as in Fig. 7, and with the same color bar for each corresponding panel. Note that we do not respect the image aspect ratio.

of the electron beam speed to the thermal speed is reduced in the mass-ratio 100 run. This reduces the strength of the Buneman and electron-electron streaming instabilties at the two RDs. The electron beam speed, due to Ampère's law, is of the order of Alfvén speed since the width of the RD is of the d_i scale. Therefore, in a regime where the electron thermal speed is larger than the Alfvén speed, or equivalently $\beta > m_e/m_i$, the instabilities at the RDs will be weak. Otherwise, when $\beta < m_e/m_i$, the instabilities at the RDs will become strong. This limit will be further studied in future papers. It is worth pointing out that if we increase the mass ratio by increasing m_i instead, the Alfvén speed will be reduced, so the ratio of the electron beam speed (scaling as the Alfvén speed) to the thermal speed will still be reduced. In Sec. IV C, we investigate the ion-ion instability in run 4.

C. Studies of ion-ion instabilities

We now explore the driver of the turbulence seen in the core of the exhaust at the SS around $y = 5$ in Figs. 9(f) and 9(h). In Figs. 10(a) and 10(c), we show a blowup of $E_{\|}$ in the y-z (at $x = 2$) and x-z (at $y = 4.6$) planes. The white lines in both panels are the same line $x = 2$, $y = 4.6$. These data reveal that the dominant wavevector is along the z direction, which is essentially the magnetic field direction at that location. Also, given that that the magnetic field perturbations there are weak (not shown), this is also an electrostatic instability. In Figs. 10(b) and 10(d), we show the ion and electron phase spaces z-V_z along the white line in Fig. 10(c). The instability partially thermalizes the counterstreaming ion beams and has only a small impact on electrons, so this appears to be a weak ion-ion streaming instability.

To establish this conclusion, we use `pdrk`[24] to show that a reasonable ion distribution function can produce the basic characteristics of the instability in the simulation. Specifically, we show that a reasonable distribution function can lead to an electrostatic instability with a maximum growth rate at the wavelength and phase speed close to that measured in the simulation. We plot this representative distribution function in Fig. 11(a). The two beams have velocities of −0.25 and 0.65 with thermal speeds of 0.35 and 0.13. The density ratio is 84:16. Compared to Fig. 10(b), we can see that the peaks of the beams and the thermal spread of this distribution function are close to those in

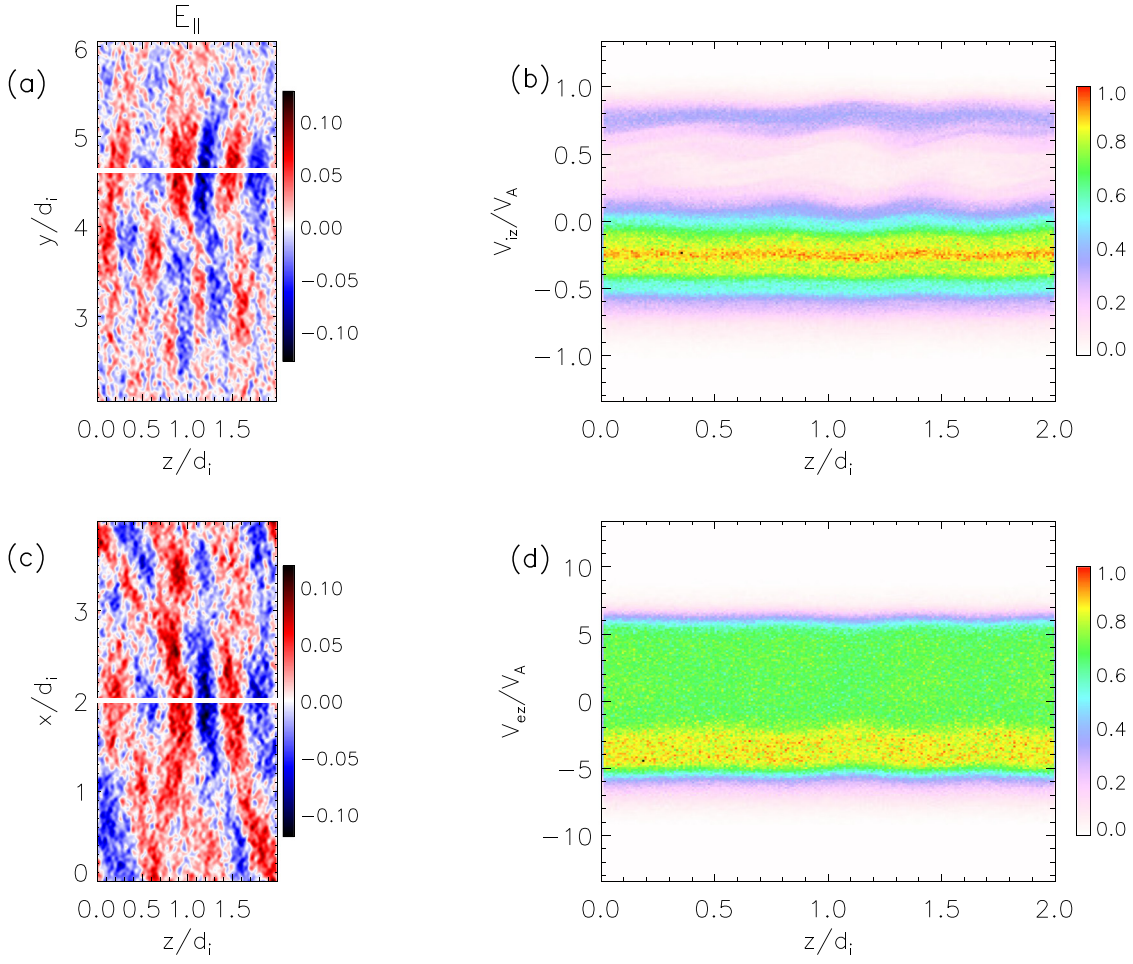

FIG. 10. In (a) and (c), a zoom into the region around $y = 5$ of run 4. Shown is $E_{\|}$ in y-z and x-z planes. In (b) and (d), the ion and electron phase space z-V_z along the white lines in (a) and (c). In (b) and (d), the color bar is normalized to the maximum value in each panel.

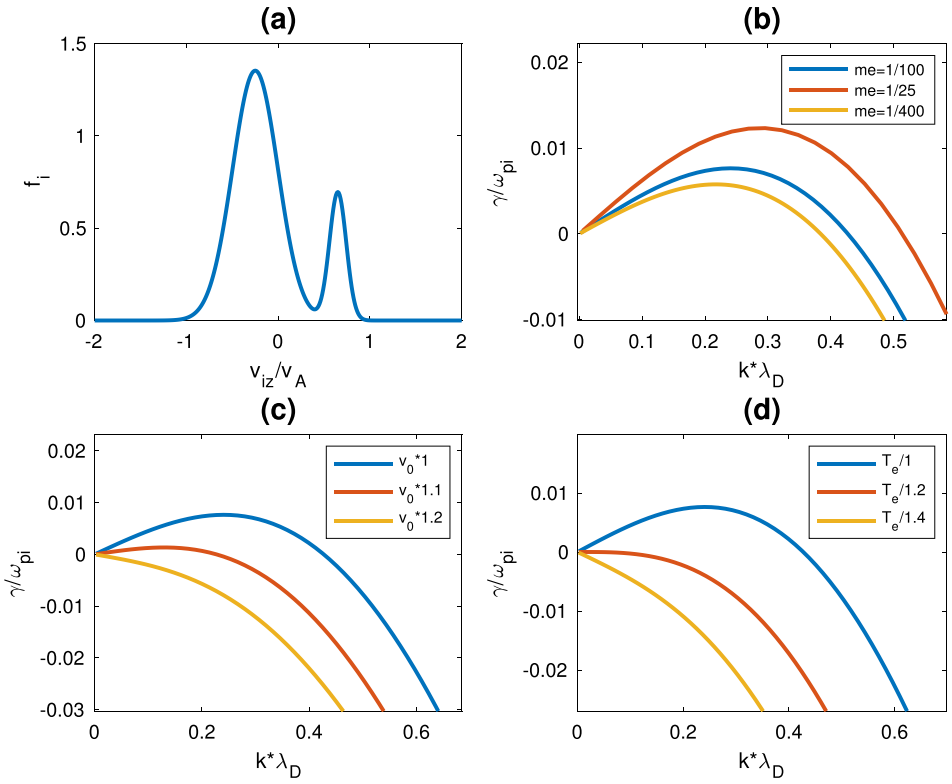

FIG. 11. In (a), a simple model of the ion distribution prior to the ion-ion instability. The growth rates γ are plotted vs k in the blue lines in (b)–(d). The dependence of γ on the mass ratio, the relative drift of the two beams, and the electron temperature are also shown.

the simulation. We use a Maxwellian distribution of electrons with an electron parallel temperature of 0.14 as measured in the simulation. Using `pdrk`, the growth rate, γ, is plotted vs k in the blue lines in Figs. 11(b)–11(d). It produces a fastest growing mode with a wavelength of about 0.67 and a phase speed of about 0.41, which is comparable to that in the simulation. Thus, the instability is driven by the counterstreaming ions. In addition, we show the dependence of γ on the mass ratio, the relative drift of the two beams, and the electron temperature. As in the simulations, the speed of light is chosen to be proportional to $1/\sqrt{m_e}$ so the electrons remain nonrelativistic. Figure 11(b) reveals that the instability weakens as the mass ratio increases, which is consistent with the simulation results. The wavelength of the fastest growing mode (normalized to the Debye length) is not sensitive to the mass ratio. If we renormalize it to d_i as in the simulations, the wavelength will be roughly proportional to $\sqrt{m_e}$, which is consistent with the simulations. Figures 11(c) and 11(d) show that a higher relative drift V_0 or lower electron temperature T_e have a stabilizing effect. With a small change of these parameters, the instability becomes stable, so the instability is close to marginal. This is consistent with the weak disturbance of the ion phase space in Figs. 10(b) and 10(d). This dependence is also consistent with the theoretical results by Fujita[25] that the instability is stabilized when the sound speed $\sqrt{T_e/m_i}$ is lower than half of the relative drift of the ion beams. In addition, as shown in Zhang *et al.*,[19] the relative speed of the counterstreaming ions in the exhaust is proportional to the Alfvén speed and the electron temperature in the exhaust is of the order of the upstream temperature. Thus, lowering the upstream sound speed to the Alfvén speed ratio (or equivalently lowering upstream β) can stabilize the instability. This is consistent with the discussion in Zhang *et al.*[19] where it was concluded that the counterstreaming ion beams would be stable in the low upstream β limit. In consequence, the counterstreaming ion beams that develop during the low β reconnection can propagate long distances before thermalizing and they are therefore unable to drive the strong turbulence necessary to produce significant dissipation at the SSs.

V. CONCLUSION

In this paper, we have used a 2D reconnection simulation, 2D and 3D Riemann simulations, and a kinetic dispersion relation solver to explore the role of instabilities and turbulence in low-β, guide-field reconnection exhausts. The overall structure of the exhaust is controlled by a pair of RDs that bound the exhaust and rotate the reconnecting field into the out-of-plane direction. The RDs drive the Alfvénic outflow exhaust and out-of-plane flows that propagate toward the center of the exhaust and drive a pair of slow shocks. The initial total plasma β in the simulations was chosen to be 0.1. The 2D reconnection and Riemann simulations reveal that just downstream of the x-line, the Buneman instability develops at the low density RD, the RD in which the electron flow supporting the magnetic rotation points toward the exhaust center. The turbulence in this RD transitions to a longer wavelength and drives electron current striations that penetrate into the core of the exhaust. Further downstream, the entire exhaust core exhibits large-amplitude striations that are linked to an oblique electron-beam-driven, electromagnetic ion cyclotron instability. The electron beam driving this instability is injected from the low density RD. However, in 3D Riemann simulations, the additional dimension

enables the growth of strong Buneman and electron-electron streaming instabilities at both RDs by allowing a nonzero k_z, which is along the strong guide field B_z. These strong instabilities suppress the generation of the electron beam at the low density RD with the consequence that the current striations in the core of the exhaust are largely suppressed. However, the instabilities at the RDs become weaker with a higher ion-to-electron mass ratio due to the higher electron thermal speed compared with the electron beam speed (of the order of the Alfvén speed). In the regime of $\beta > m_e/m_i$, the electron thermal speed is larger than the Alfvén speed and these instabilities will be weak. Otherwise, they will be strong. The strong turbulence regime of $\beta < m_e/m_i$ will be further explored in the future. In addition to the Buneman and electron-electron streaming instabilities at the two RD current sheets, the 3D simulation also reveals an ion-ion streaming instability in the core of the exhaust at the SSs which acts to partially thermalize the counter-streaming ion beams that generate the SSs. We use a kinetic dispersion relation solver to show the ion streaming instability is stable when the Alfvén speed greatly exceeds the ion sound speed at a low upstream β. The consequence is the counterstreaming ion beams that develop during the low β reconnection can propagate long distances before thermalizing and they are therefore incapable of driving the strong turbulence necessary to produce significant dissipation at the SSs. The direct exploration of the very low β regime to further establish the stability of the counterstreaming ion beams is a topic for future work.

The results suggest that in realistic low-β guide field reconnection exhausts with upstream $\beta > m_e/m_i$, the slow shocks inside the exhaust are largely laminar and the instabilities and turbulence that develop will likely be too weak to play a significant role in energy conversion. Without strong turbulence at the slow shocks, neither species can undergo the canonical diffusive shock acceleration. Energy conversion in the exhaust will be dominantly controlled by laminar physics with little dissipation or scattering from turbulence. The results are therefore consistent with the conclusions by Zhang *et al.*[19] This conclusion has broad implications for understanding reconnection in the solar corona and the inner heliosphere. The types and roles of the instabilities and turbulence can be tested from the data expected from the Parker Solar Probe[26,27] as it approaches the low-β environment in the outer reaches of the solar corona.

ACKNOWLEDGMENTS

This work was supported by NSF Grant Nos. PHY1805829 and PHY1500460, NASA Grant Nos. NNX14AC78G and NNX17AG27G, and the FIELDS Team of the Parker Solar Probe (NASA Contract No. NNN06AA01C). The simulations were carried out at the National Energy Research Scientific Computing Center. The simulation data are available on request.

REFERENCES

[1]J. F. Drake, M. Swisdak, C. Cattell, M. A. Shay, B. N. Rogers, and A. Zeiler, Science **299**, 873 (2003).
[2]C. Cattell, J. Dombeck, J. Wygant, J. F. Drake, M. Swisdak, M. L. Goldstein, W. Keith, A. Fazakerley, M. André, E. Lucek, and A. Balogh, J. Geophys. Res.: Space Phys. **110**, A01211, https://doi.org/10.1029/2004JA010519 (2005).
[3]H. Che, J. F. Drake, and M. Swisdak, Nature **474**, 184 (2011).
[4]D. B. Graham, Y. V. Khotyaintsev, C. Norgren, A. Vaivads, M. André, S. Toledo-Redondo, P.-A. Lindqvist, G. T. Marklund, R. E. Ergun, W. R. Paterson, D. J. Gershman, B. L. Giles, C. J. Pollock, J. C. Dorelli, L. A. Avanov, B. Lavraud, Y. Saito, W. Magnes, C. T. Russell, R. J. Strangeway, R. B. Torbert, and J. L. Burch, J. Geophys. Res.: Space Phys. **122**, 517, https://doi.org/10.1002/2016JA023572 (2017).
[5]L. Price, M. Swisdak, J. F. Drake, P. A. Cassak, J. T. Dahlin, and R. E. Ergun, Geophys. Res. Lett. **43**, 6020, https://doi.org/10.1002/2016GL069578 (2016).
[6]A. Le, W. Daughton, L.-J. Chen, and J. Egedal, Geophys. Res. Lett. **44**, 2096, https://doi.org/10.1002/2017GL072522 (2017).
[7]L. Price, M. Swisdak, J. F. Drake, J. L. Burch, P. A. Cassak, and R. E. Ergun, J. Geophys. Res.: Space Phys. **122**(11), 11086, https://doi.org/10.1002/2017JA024227 (2017).
[8]Y.-H. Liu, J. F. Drake, and M. Swisdak, Phys. Plasmas **19**, 022110 (2012).
[9]P. A. Muñoz and J. Büchner, Phys. Plasmas **23**, 102103 (2016).
[10]F. Pucci, S. Servidio, L. Sorriso-Valvo, V. Olshevsky, W. H. Matthaeus, F. Malara, M. V. Goldman, D. L. Newman, and G. Lapenta, Astrophys. J. **841**, 60 (2017).
[11]J. P. Eastwood, R. Mistry, T. D. Phan, S. J. Schwartz, R. E. Ergun, J. F. Drake, M. Øieroset, J. E. Stawarz, M. V. Goldman, C. Haggerty, M. A. Shay, J. L. Burch, D. J. Gershman, B. L. Giles, P. A. Lindqvist, R. B. Torbert, R. J. Strangeway, and C. T. Russell, Geophys. Res. Lett. **45**, 4569, https://doi.org/10.1029/2018GL077670 (2018).
[12]H. Jiansen, Z. Xingyu, C. Yajie, S. Chadi, S. Michael, L. Hui, R. Wenzhi, Z. Lei, and T. Chuanyi, Astrophys. J. **856**, 148 (2018).
[13]Y. Lin and L. C. Lee, Space Sci. Rev. **65**, 59 (1993).
[14]M. Scholer and R.-F. Lottermoser, Geophys. Res. Lett. **25**, 3281, https://doi.org/10.1029/98GL52510 (1998).
[15]M. Cremer and M. Scholer, Geophys. Res. Lett. **26**, 2709, https://doi.org/10.1029/1999GL900592 (1999).
[16]M. Cremer and M. Scholer, J. Geophys. Res.: Space Phys. **105**, 27621, https://doi.org/10.1029/2000JA000196 (2000).
[17]Y.-H. Liu, J. F. Drake, and M. Swisdak, Phys. Plasmas **18**, 062110 (2011).
[18]Y.-H. Liu, J. F. Drake, and M. Swisdak, Phys. Plasmas **18**, 092102 (2011).
[19]Q. Zhang, J. F. Drake, and M. Swisdak, Phys. Plasmas **26**, 72115 (2019).
[20]M. E. Innocenti, M. Goldman, D. Newman, S. Markidis, and G. Lapenta, Astrophys. J. **810**, L19 (2015).
[21]M. E. Innocenti, E. Cazzola, R. Mistry, J. P. Eastwood, M. V. Goldman, D. L. Newman, S. Markidis, and G. Lapenta, Geophys. Res. Lett. **44**, 3447, https://doi.org/10.1002/2017GL073092 (2017).
[22]W. E. Drummond and M. N. Rosenbluth, Phys. Fluids **5**, 1507 (1962).
[23]A. Zeiler, D. Biskamp, J. F. Drake, B. N. Rogers, M. A. Shay, and M. Scholer, J. Geophys. Res.: Space Phys. **107**, SMP 6-1, https://doi.org/10.1029/2001JA000287 (2002).
[24]H. Xie and Y. Xiao, Plasma Sci. Technol. **18**, 97 (2016).
[25]T. Fujita, T. Ohnuma, and S. Adach, Plasma Phys. **19**, 875 (1977).
[26]S. D. Bale, K. Goetz, P. R. Harvey, P. Turin, J. W. Bonnell, T. Dudok de Wit, R. E. Ergun, R. J. MacDowall, M. Pulupa, M. Andre, M. Bolton, J.-L. Bougeret, T. A. Bowen, D. Burgess, C. A. Cattell, B. D. G. Chandran, C. C. Chaston, C. H. K. Chen, M. K. Choi, J. E. Connerney, S. Cranmer, M. Diaz-Aguado, W. Donakowski, J. F. Drake, W. M. Farrell, P. Fergeau, J. Fermin, J. Fischer, N. Fox, D. Glaser, M. Goldstein, D. Gordon, E. Hanson, S. E. Harris, L. M. Hayes, J. J. Hinze, J. V. Hollweg, T. S. Horbury, R. A. Howard, V. Hoxie, G. Jannet, M. Karlsson, J. C. Kasper, P. J. Kellogg, M. Kien, J. A. Klimchuk, V. V. Krasnoselskikh, S. Krucker, J. J. Lynch, M. Maksimovic, D. M. Malaspina, S. Marker, P. Martin, J. Martinez-Oliveros, J. McCauley, D. J. McComas, T. McDonald, N. Meyer-Vernet, M. Moncuquet, S. J. Monson, F. S. Mozer, S. D. Murphy, J. Odom, R. Oliverson, J. Olson, E. N. Parker, D. Pankow, T. Phan, E. Quataert, T. Quinn, S. W. Ruplin, C. Salem, D. Seitz, D. A. Sheppard, A. Siy, K. Stevens, D. Summers, A. Szabo, M. Timofeeva, A. Vaivads, M. Velli, A. Yehle, D. Werthimer, and J. R. Wygant, Space Sci. Rev. **204**, 49 (2016).
[27]J. C. Kasper, R. Abiad, G. Austin, M. Balat-Pichelin, S. D. Bale, J. W. Belcher, P. Berg, H. Bergner, M. Berthomier, J. Bookbinder, E. Brodu, D. Caldwell, A. W. Case, B. D. G. Chandran, P. Cheimets, J. W. Cirtain, S. R. Cranmer, D. W. Curtis, P. Daigneau, G. Dalton, B. Dasgupta, D. DeTomaso, M. Diaz-Aguado, B. Djordjevic, B. Donaskowski, M. Effinger, V. Florinski, N. Fox, M. Freeman, D. Gallagher, S. P. Gary, T. Gauron, R. Gates, M. Goldstein, L. Golub, D. A. Gordon, R. Gurnee, G. Guth, J. Halekas, K. Hatch, J. Heerikuisen, G. Ho, Q. Hu, G. Johnson, S. P. Jordan, K. E. Korreck, D. Larson, A. J. Lazarus, G. Li, R. Livi, M. Ludlam, M. Maksimovic, J. P. McFadden, W. Marchant, B. A. Maruca, D. J. McComas, L. Messina, T. Mercer, S. Park, A. M. Peddie, N. Pogorelov, M. J. Reinhart, J. D. Richardson, M. Robinson, I. Rosen, R. M. Skoug, A. Slagle, J. T. Steinberg, M. L. Stevens, A. Szabo, E. R. Taylor, C. Tiu, P. Turin, M. Velli, G. Webb, P. Whittlesey, K. Wright, S. T. Wu, and G. Zank, Space Sci. Rev. **204**, 131 (2016).